INORGANIC CHEMISTRY FRONTIERS

CHINESE CHEMICAL SOCIETY

ROYAL SOCIETY OF CHEMISTRY

RESEARCH ARTICLE

View Article Online
View Journal

Cite this: DOI: 10.1039/d5qi00001g

A bifunctional antioxidant for concurrent enhancement of stability and zinc-ion storage properties of $Ti_3C_2T_x$†

Jie Wang, Guohao Li, Hailiang He, Xiaohui Li, Jiale Fan, Yingxinjie Wang, Xiuqiang Xie * and Nan Zhang *

MXenes exhibit exceptional physicochemical properties, rendering them highly promising for applications in electrochemical energy storage devices. However, their easy oxidation and inherent tendency for self-stacking pose significant challenges, thereby limiting their utilization in practical applications. In this study, sodium sulfide (Na_2S) was used to enhance the stability of $Ti_3C_2T_x$ under multiple environmental conditions. Additionally, compared to the reported antioxidants such as ascorbic acid (VC), sodium borohydride ($NaBH_4$), sodium ascorbate (NaAc), and sodium bisulfite ($NaHSO_3$), Na_2S possesses an appropriate level of reducing strength and was further used as the reducing agent to fabricate 3D macro-porous $Ti_3C_2T_x$/reduced graphene oxide (SMG) hydrogels at room temperature. This prevents the oxidation of $Ti_3C_2T_x$, which occurs during the traditional heated gelation process, and generates a porous structure conducive to ion transport. As a free-standing cathode for zinc-ion storage, the SMG electrode exhibits a high areal specific capacity of 526.2 mF cm^{-2} at 2 mA cm^{-2}, much higher than that of the $Ti_3C_2T_x$/graphene oxide film (MG, 111.4 mF cm^{-2}), together with outstanding cycling performance (83.6% capacity retention after 30 000 cycles). This study presents Na_2S as a bifunctional antioxidant for enhancing the stability of MXenes and constructing 3D MXene-based aerogels at room temperature with exceptional zinc storage performance.

Received 1st January 2025,
Accepted 22nd April 2025

DOI: 10.1039/d5qi00001g

rsc.li/frontiers-inorganic

Introduction

MXenes, a family of two-dimensional (2D) transition metal carbides and/or nitrides, have garnered immense interest in the field of energy storage owing to their exceptional physicochemical properties, including high conductivity, large surface area, and tunable interlayer spacers.[1–3] The hydrophilic nature of MXenes, imparted by the surface terminal groups (*e.g.*, –O–, –OH, –F), allows for facile ion intercalation/deintercalation, making them ideally suited for aquatic energy storage applications.[4–6] These devices rely on MXenes to accommodate ions with substantial energy density. However, MXene flakes exhibit high susceptibility to oxidation, leading to the deterioration of their 2D structure and the consequent loss of functional properties.[7–9] Additionally, like other 2D materials, MXene nanosheets are susceptible to face-to-face self-restacking and aggregation, which causes a considerable decrease in electrochemical active sites and impairs ion transport/diffusion kinetics. To fully realize their potential in energy storage, the development of MXene materials with high storage stability and an open three-dimensional (3D) structure to facilitate rapid ion transport and enhance surface utilization is the primary direction for developing MXene-based electrodes.

The stability of MXenes, particularly their susceptibility to oxidation under ambient conditions, poses a significant challenge for practical applications. Research on improving the storage stability of MXenes is emerging. L-Ascorbate and polyanionic salts are used to protect the edge of $Ti_3C_2T_x$ and restrict water molecules from approaching the active site.[10,11] The hydration effect of high-concentration inorganic salts significantly reduces water activity and dissolved oxygen intensity to significantly improve the storage stability of $Ti_3C_2T_x$.[12] However, the addition of these antioxidants enhances the stability of MXenes without introducing any other significant advantages. Recently, the *in situ* surface chemistry strategy utilizing oxyanion terminations has shown promising potential in enhancing the self-antioxidant capability. This strategy also facilitates the formation of stable and uniform $Ti_3C_2T_x$ inks, characterized by controlled rheological properties and excellent processability.[13] Such dual-purpose strategies, which can simultaneously enhance the stability of MXenes and function-

---

College of Materials Science and Engineering, Hunan University, Changsha 410082, China. E-mail: xiuqiang_xie@hnu.edu.cn, nanzhang@hnu.edu.cn

† Electronic supplementary information (ESI) available. See DOI: **https://doi.org/10.1039/d5qi00001g**

ally modify them, are uncommon, especially in the synthesis of 3D MXene materials. Therefore, exploring multifunctional antioxidants is worthwhile to fully harness the unique properties and characteristics of MXenes.

In this study, versatile sodium sulfide (Na_2S) is chosen as an antioxidant to improve the stability of MXenes under multiple environmental conditions. Furthermore, Na_2S is employed as a reductant to facilitate the easy synthesis of the $Ti_3C_2T_x$ MXene/reduced graphene oxide (rGO) (SMG) hydrogel at room temperature, which avoids the possible oxidation issues associated with heating in conventional hydrogel preparation. Here, Na_2S exhibits a more suitable reduction strength than ascorbic acid (VC), sodium borohydride ($NaBH_4$), sodium ascorbate (NaAc), and sodium bisulfite ($NaHSO_3$), effectively promoting the reduction of graphene oxide (GO). The reduction mechanism involves the cleavage of the epoxy bonds in GO to form pendant oxygen bonds, which subsequently undergo crosslinking with $Ti_3C_2T_x$, ultimately leading to the formation of SMG. The obtained SMG hydrogel is more stable than the MXene/GO (MG) solution. Additionally, SMG exhibits a 3D channel structure, which enhances the charge-transport properties. When served as the cathode of a zinc-ion hybrid supercapacitor (ZHSC), the SMG electrode exhibits a remarkable areal specific capacitance of 526.2 mF cm^{-2} at 2 mA cm^{-2} and exceptional cycling stability, with a capacitance retention of 83.6% after 30 000 cycles. Our strategy provides novel insights into the development of bifunctional antioxidants that concurrently enhance the stability and functional properties of MXenes, thereby contributing to the broadened application and durability of MXenes.

Experimental section

Preparation of $Ti_3C_2T_x$ nanosheets

$Ti_3C_2T_x$ nanosheets were prepared according to our previous report.[14]

Stability test for $Ti_3C_2T_x$ colloidal solution with the protection of Na_2S

Na_2S was dissolved in $Ti_3C_2T_x$ colloid in a 20 mL sealed glass vial, with both Na_2S and $Ti_3C_2T_x$ having a concentration of 1 mg mL^{-1}. The vial was then stored at room temperature in the dark. Upon utilization, the MXene was separated from the salt solution through several centrifugation steps, followed by rinsing with water and freeze-drying for further analysis.

Synthesis of the SMG aerogels and MG films

A colloidal mixture of $Ti_3C_2T_x$ (4.5 mL at 5 mg mL^{-1}) and GO (1.5 mL at 5 mg mL^{-1}) was combined in a 20 mL glass vial. This blend was vigorously stirred for 30 min and then sonicated for 1 min. Next, 15 mg of Na_2S was added to the colloidal mixture, which was stirred for an additional 30 min and sonicated for 1 min. Subsequently, the vial was left undisturbed at 25 °C for 72 h to facilitate the formation of the SMG hydrogel. The obtained hydrogel was rinsed with deionized water to eliminate excess reactants or impurities. Following freeze-drying, the SMG aerogel was obtained. For comparison, the MG film was prepared by vacuum filtration of a $Ti_3C_2T_x$ (4.5 mL at 5 mg mL^{-1}) and GO (1.5 mL at 5 mg mL^{-1}) colloidal mixture.

Characterization

The morphological analysis was performed using a JSM-6700F spectrophotometer employing field emission scanning electron microscopy (FE-SEM) techniques. A JEOL Jem 2010 EX instrument was employed to obtain TEM images, operating at an accelerating voltage of 200 eV. The XRD analyses were performed on a Bruker D8 Advance X-ray diffractometer, equipped with Ni-filtered Cu Kα radiation, scanning at a rate of 0.2° s^{-1}. XPS testing was conducted using a Kratos Axis Supra system using an ESCALAB 250 spectrometer from PerkinElmer. Raman spectroscopy was carried out using the LabRM Aramis Raman system. The electrical conductivities were measured using a 4-point probe resistivity measurement system (Guangzhou Four Probe Technology Co., Ltd), featuring a consistent probe spacing of 1.0 mm. Additionally, the zeta potentials (ζ) were measured using a dynamic light scattering analyzer (Zetasizer 3000HSA).

Electrochemical measurement

The electrochemical performance was evaluated using coin-type cells, which consisted of an MXene-based electrode serving as the cathode, a commercial Zn foil as the anode, a glass fiber membrane as the separator, and a 2 M $ZnSO_4$ aqueous electrolyte solution. The mass loading of the electrode was about 1.0 mg cm^{-2}. CV, GCD, and EIS measurements were acquired using a CHI 660E workstation. The long-term cycling stability of the cells was assessed using a Neware battery test system. The area capacitance (C_{areal}) was determined through galvanostatic charge/discharge curves using the following formula:

$$C_{\mathrm{areal}} = \frac{It}{S\Delta V}$$

where I represents the constant discharge current (A), t is the discharge time (s), S denotes the total area of the electrode (cm^{-2}), and ΔV signifies the voltage range.

Results and discussion

The colloidal dispersions of $Ti_3C_2T_x$ were mixed with an aqueous Na_2S solution, an essential antioxidant fostering a reducing environment. These Na_2S-stabilized $Ti_3C_2T_x$ dispersions (designated as SM) and their pure $Ti_3C_2T_x$ counterpart (designated as M) were carefully sealed in bottles and stored at ambient temperature for 28 days. The SEM image in Fig. 1A reveals a densely populated nanoparticle surface on M, indicative of substantial oxidation, which is also observed in the TEM images (Fig. 1B). The corresponding selected area diffraction patterns (SAED) are displayed in Fig. 1C. All the diffraction

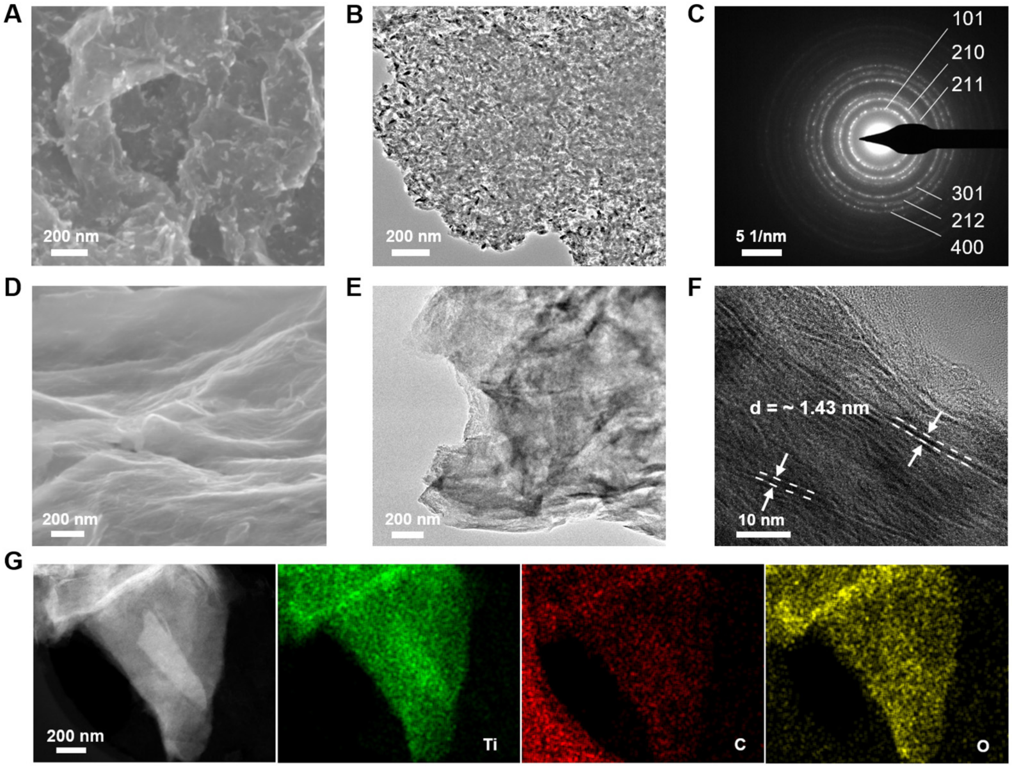

Fig. 1 Typical (A) SEM, (B) TEM and (C) SAED images of M. Typical (D) SEM, (E) TEM, (F) HR-TEM images, and (G) HAADF-STEM image with the corresponding elemental mapping images of SM stored after 28 days.

rings are attributed to TiO_2, confirming the severe oxidation of $Ti_3C_2T_x$. Conversely, at the same magnification, SM exhibits a distinct nanosheet morphology, characterized by a relatively smooth surface in both SEM (Fig. 1D) and TEM (Fig. 1E) images. As depicted in Fig. 1F, the high-resolution TEM image reveals lattice spacings of ~1.43 nm, which align with the (002) lattice plane of $Ti_3C_2T_x$. Furthermore, through the application of high-angle annular dark-field scanning transmission electron microscopy (HAADF-STEM) in Fig. 1G, complemented by additional elemental mapping techniques, it is demonstrated that titanium (Ti), carbon (C), and oxygen (O) are uniformly distributed across the entire $Ti_3C_2T_x$ MXene nanosheet.

The stability of M and SM after 28 days of storage is further investigated. As shown in Fig. 2A, SM maintains the characteristic (002) peak of $Ti_3C_2T_x$ at a 2θ of approximately 6.2° in the XRD pattern, corresponding to the interlayer spacing of 1.43 nm, which is well aligned with the TEM results. No obvious oxidation peak indicates that the structure is preserved. In contrast, the (002) peak of M significantly weakens, accompanied by the emergence of new peaks at 27.4°, 35.6°, 40.7°, and 53.7°, corresponding to the rutile TiO_2 phase (JCPDS no. 76-0323), suggesting the obvious oxidation of $Ti_3C_2T_x$. Moreover, Raman spectroscopic analysis of the samples was conducted systematically. As shown in Fig. 2B, the Raman spectrum of SM displays distinct peaks associated with $Ti_3C_2T_x$, including the A_{1g} mode at 198 cm^{-1} for carbon and the E_g mode at 378 and 614 cm^{-1} for Ti and surface functional groups.[15] As for M, the oxidation is evident from the prominent B_{1g} peak of TiO_2 at 160 cm^{-1}.[16] Both the XRD and Raman spectroscopic analyses indicate the efficacy of Na_2S in maintaining the crystalline integrity of the $Ti_3C_2T_x$ nanosheets. To gain a more profound understanding of how Na_2S affects the oxidation states of Ti within $Ti_3C_2T_x$ nanosheets, high-resolution XPS of the Ti 2p region was performed (Fig. 2C) and Fig. S1† compares the relative atomic percentages of Ti species (Ti–C, Ti^{2+}, Ti^{3+}, and Ti^{4+}) in aged aqueous $Ti_3C_2T_x$ dispersions.[17] As expected, the proportion of Ti species with high oxidation valence in SM is lower than that in M. Concretely, the Ti^{4+} content within the Ti 2p region supported by the high-intensity peaks at 464 and 458 eV of M is approximately 30.5%, whereas SM exhibits a markedly lower Ti^{4+} content of around 12.3%, indicative of the effective protection by Na_2S. Additionally, no peak appears in the high-resolution S 2p XPS spectra of SM in Fig. S2.† The results indicate that the protective effect arises not from a direct interaction between Na_2S and $Ti_3C_2T_x$ but rather from the reductive environment originating from Na_2S, which mitigates the effect of potential oxidizing agents.

Furthermore, the electrical conductivity was measured to assess structural integrity.[18,19] As shown in Fig. 2D, M displays a notably reduced electrical conductivity of 833.3 S cm^{-1} after 28 days of storage, significantly lower than its initial value of 2000 S cm^{-1}. In contrast, SM demonstrates a comparable electrical conductivity of 1667 S cm^{-1} after the same storage

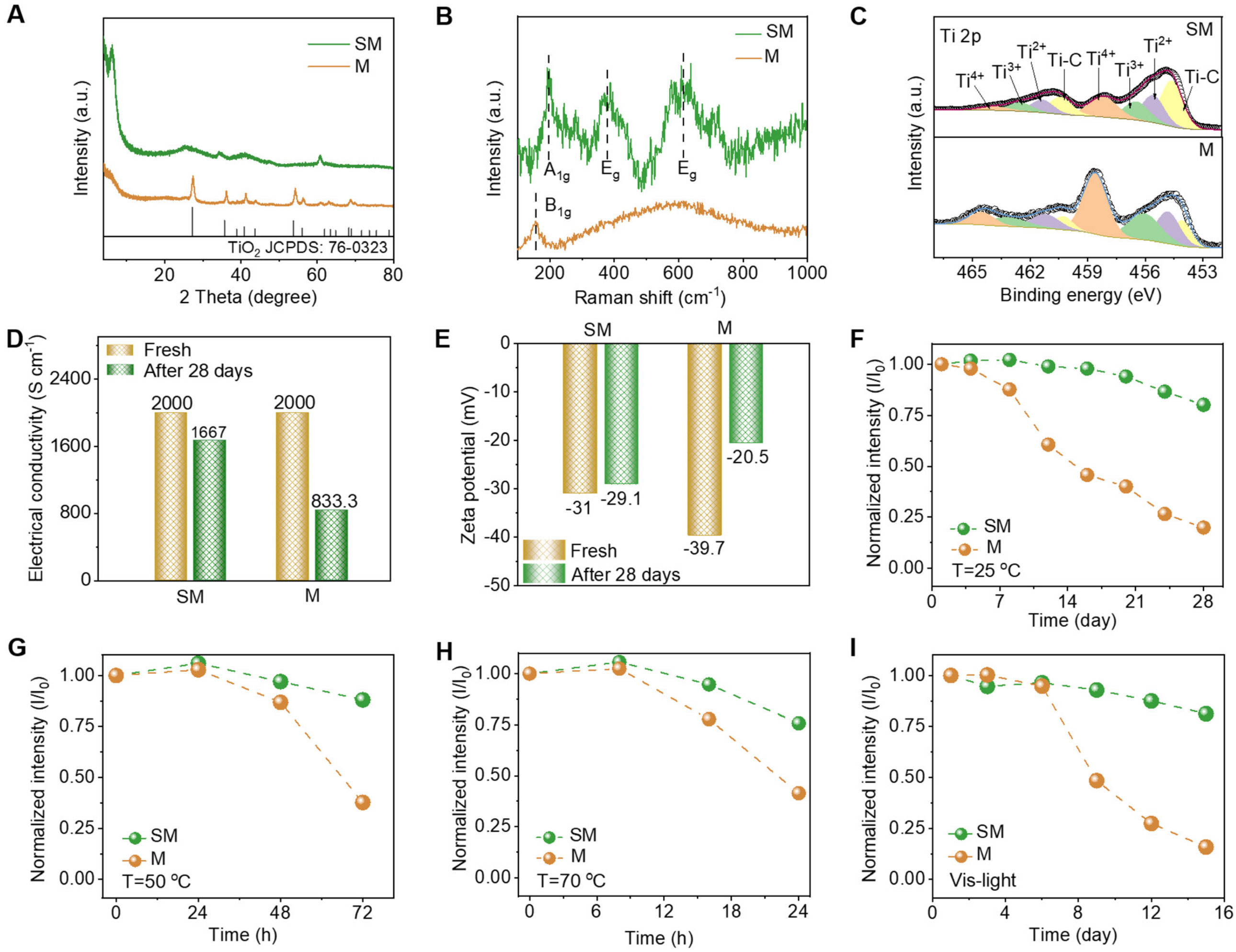

Fig. 2 Characterization of M and SM after storing for 28 days. (A) XRD, (B) Raman, and (C) XPS patterns of M and SM. (D) Electrical conductivity and (E) zeta potentials (ζ) of SM and M. The normalized intensity of the peak observed in UV-Vis absorption spectroscopy at ~780 nm for both SM and M samples, measured at temperatures of (F) 25 °C, (G) 50 °C, and (H) 70 °C, and (I) under visible light irradiation.

period. This remarkable stability in conductivity is attributed to the effective suppression of oxidation processes. Zeta potentials (ζ) were employed as a tool to investigate the stability characteristics of $Ti_3C_2T_x$ dispersions.[20] As evident from Fig. 2E, a significant reduction in the ζ value of M, from −39.7 to −20.5 mV, is observed, which is the result of the oxidation.[21] Notably, SM exhibits a remarkably stable ζ value of approximately −29.1 mV even after a prolonged storage period of 28 days, which is close to its fresh state value of −31 mV, also providing compelling evidence for the antioxidative efficacy of Na_2S. The effective preservation of negative functional groups on the surface of $Ti_3C_2T_x$ facilitates seamless reprocessing post-storage, which provides Na_2S-mediated protection strategies with great potential for applications. The oxidation stability of the $Ti_3C_2T_x$ colloidal suspension was also assessed through UV-Vis absorption spectroscopy. To assess the progress of oxidation over time, the I/I_0 ratio was tracked, where I represents the peak intensity at ~780 nm at a given time interval and I_0 is the initial peak intensity.[14] As shown in Fig. 2F, the I/I_0 ratio for M decreases swiftly to approximately 20% within 28 days, indicative of its rapid oxidation and subsequent degradation. In contrast, the degradation of $Ti_3C_2T_x$ is significantly reduced upon introducing Na_2S into the aqueous medium. Specifically, the I/I_0 ratio of SM is 80%, suggesting the slow oxidation kinetics brought by the protection of Na_2S. Even after being stored at 50 °C for 72 hours and at 70 °C for 24 hours (Fig. 2G and H), SM retains 88.0% and 75.7% of its initial state, respectively, far surpassing the performance of M (37.7% and 41.4%), which highlights the superior stability imparted by Na_2S treatment. Considering that light irradiation accelerates the oxidation of $Ti_3C_2T_x$,[19] the stabilizing effect of Na_2S under visible light exposure was further evaluated. As shown in Fig. 2I after 15 days of continuous visible light irradiation, M retains a mere 15% of its initial intensity, whereas SM maintains a remarkable 81%, thereby unlocking the potential for storage and application of $Ti_3C_2T_x$ under illuminated conditions, including photocatalytic reactions and solar desalination processes.

Taking advantage of the reducing properties of Na_2S, SMG was synthesized at room temperature. In this way, MXene is less prone to oxidation at room temperature compared with traditional heating methods. The schematic illustration for the synthesis of SMG hydrogel is depicted in Fig. 3A. Firstly, MXene and GO colloidal suspensions are mixed in a glass vial and vigorously stirred to ensure a homogeneous MXene/GO hybrid suspension is obtained. Upon the introduction of Na_2S into the MXene/GO colloidal suspensions, the GO transforms into rGO *via* a primarily Na_2S-mediated reduction process. This transformation involves the ring-opening of epoxy groups on the GO to form oxygen dangling bonds, which contribute to the crosslinking of MXene and rGO nanosheets.[22] Meanwhile, partial hydrophilic oxygen-containing functional groups are eliminated, thereby enhancing the hydrophobicity of the rGO and partially restoring its π-conjugated structural integrity.[23] Two potential types of interactions are present within the SMG hydrogel system: (a) hydrogen bonding between functional groups, including –OH, –F, –O–, and –COOH, located on adjacent nanosheets, and (b) π–π stacking interactions occurring between rGO nanosheets. The fine balance between the hydrophilic and hydrophobic properties, along with the interactions, facilitates the assembly of rGO into a 3D framework. Combined with the van der Waals forces and hydrogen bonds formed between rGO and MXenes, MXene nanosheets undergo self-convergence and are incorporated into the rGO framework. The redox potential of reducing agents critically governs the hierarchical assembly of 3D architectures. Linear sweep voltammetry reveals that the reduction strength of Na_2S is weaker than that of $NaBH_4$, while it is stronger than those of NaAc, VC, $NaHSO_3$, and NaCl (Fig. S3†). As shown in Fig. S4,† when utilizing a potent reductant such as $NaBH_4$ or a weaker one like $NaHSO_3$, the resultant MXene and rGO mixture exhibits a disrupted or unstable structure, attributed to either excessive or insufficient reduction.[22] In the case of NaAc and VC, carboxyl groups undergo preferential removal rather than the formation of oxygen dangling bonds through oxygen ring-opening reactions,[24] which limits the crosslinking of $Ti_3C_2T_x$ and rGO. The fact that the addition of NaCl does not form a gel rules out the role of sodium ions. This integration gives rise to the formation of a 3D macroporous SMG hydrogel, with Na_2S serving as the primary redu-

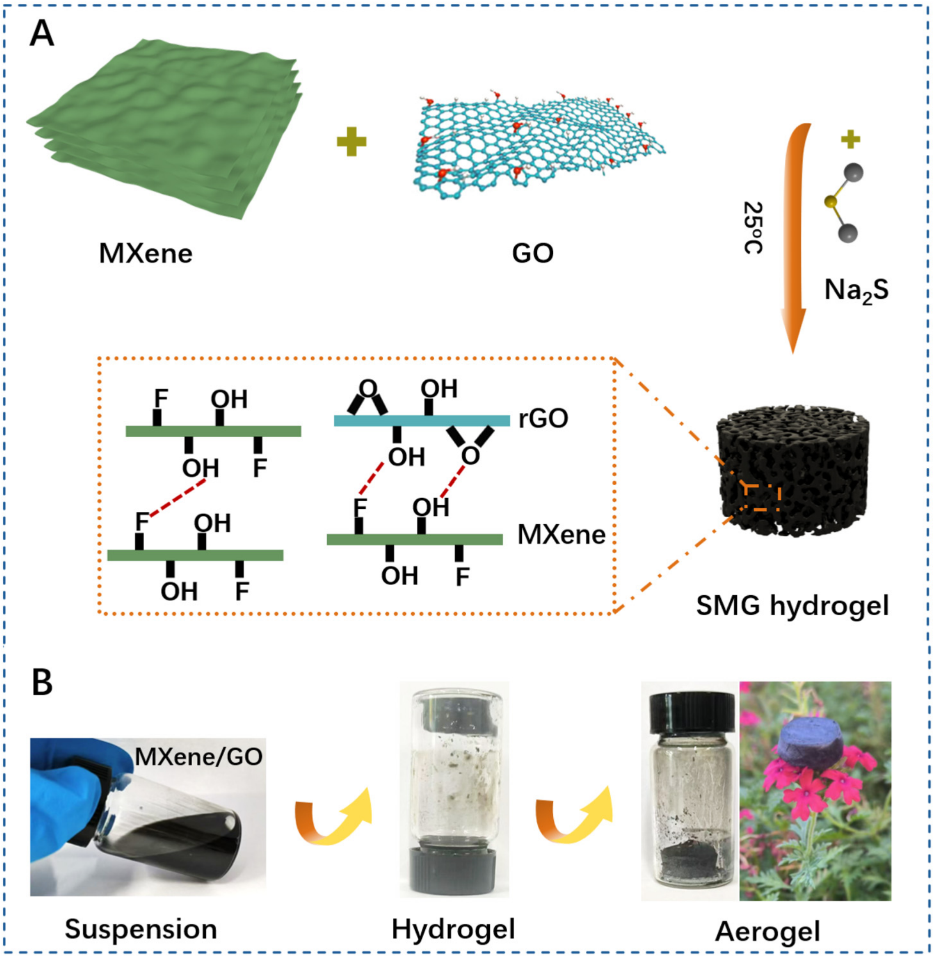

Fig. 3 (A) Schematic diagram of the formation process of the SMG hydrogel. (B) Optical photographs of morphological changes in the MXene/GO suspension and SMG aerogel.

cing agent in the crosslinking of MXene nanosheets with rGO nanosheets. The SMG aerogels are further obtained *via* freeze-drying (Fig. 3B), and the self-supporting films (MG) obtained by extracting and filtering the MXene/GO mixture are used as comparison.

To further investigate the crystal structure and surface chemistry of the samples, XRD and Raman spectra were recorded. Fig. 4A shows the XRD patterns of SMG and MG. Notably, the (002) diffraction peak shifts from 5.9° for MG to 5.6° for SMG, suggesting an expansion in the interlayer spacing from 1.49 nm to 1.57 nm. The Raman spectra of SMG and MG are shown in Fig. 4B. Below 800 cm^{-1}, SMG and MG exhibit similar out-of-plane and in-plane vibration patterns. Specifically, the Raman vibration peak at 198 cm^{-1} is assigned to the A_{1g} symmetric out-of-plane vibrations of C atoms. The modes at 395 cm^{-1} and 594 cm^{-1} correspond to the E_g vibrations, which represent in-plane vibration modes of Ti, and surface terminal group atoms.[12] Additionally, the D peak, located at 1324 cm^{-1}, is associated with defects in graphene, and the G peak, located at 1575 cm^{-1}, relates to in-plane vibrations of sp^2 carbon atoms.[25] It is evident that the D peak of MG is stronger than its G peak, while the G peak of SMG is stronger than its D peak. This indicates the presence of rGO in the prepared 3D aerogels and that the π–π interaction is enhanced.[25] Importantly, no TiO_2 vibration peaks were detected, further confirming the successful inhibition of MXene oxidation. XPS was used to investigate the surface chemistry of SMG. As shown in Fig. S5,† the XPS survey spectrum reveals that the predominant elements of SMG are C, Ti, O, F, Na and S, where the Na and S elements stem from Na_2S. As for MG, it displays the C, Ti, O, and F elements. From the high-resolution Ti 2p spectra, the Ti^{4+} peak at 459/465 eV was distinctly observed for SMG (Fig. S6†), indicative of the surface oxidation of $Ti_3C_2T_x$ facilitated by the functional groups of the GO layers. This observation confirms the interaction between $Ti_3C_2T_x$ and GO sheets at the sites of oxygen dangling bonds.[26,27] However, the XRD pattern and Raman spectrum exhibited no characteristic peaks of TiO_2 (Fig. 4A and B), suggesting that the enhancement of the Ti^{4+} peak primarily arises from the crosslinking between $Ti_3C_2T_x$ and GO. Furthermore, the high-resolution XPS spectrum of the S 2p region for SMG is shown in Fig. S7.† The binding energies at 164.6 eV and 163.2 eV correspond to S $2p_{1/2}$ and $2p_{3/2}$ of S^{2-}.[28] Additionally, the binding energies at 169.4 eV and 168.2 eV correspond to $2p_{1/2}$ and $2p_{3/2}$ of S in higher oxidation states,[29] which are sulphate species arising from the oxidation of Na_2S during the reduction of GO. This suggests that Na_2S is involved in the gelation process, which is conducive to stabilizing Ti and improving overall stability. After storing the samples in H_2O for 15 days, the XRD and Raman analyses (Fig. S8†) of MG reveal the presence of TiO_2. Conversely, the SMG sample exhibits remarkable preservation of the structural integrity of $Ti_3C_2T_x$, which is beneficial for enhancing the stability of MXenes during aqueous zinc-ion storage.

Furthermore, Fig. 4C displays the pore size distribution curves for the MG and SMG samples. The average pore size of SMG is 6.3 nm, which is greater than the 5.9 nm pore size of MG, indicating an expanded ion channel for energy storage due to the 3D assembly. BET analysis reveals that SMG exhibits a specific surface area of 27.6 m^2 g^{-1} (Fig. S9†), which is lower than that of MG (39.5 m^2 g^{-1}). This observed reduction can be attributed to the interlayer contraction and restacking phenomenon occurring during the chemical reduction of GO.[30,31] Fig. S10† shows that the MG film is dense and slightly wrinkled on the surface. After the treatment with Na_2S, SMG displays a 3D porous structure, which is attributed to the crosslinking of

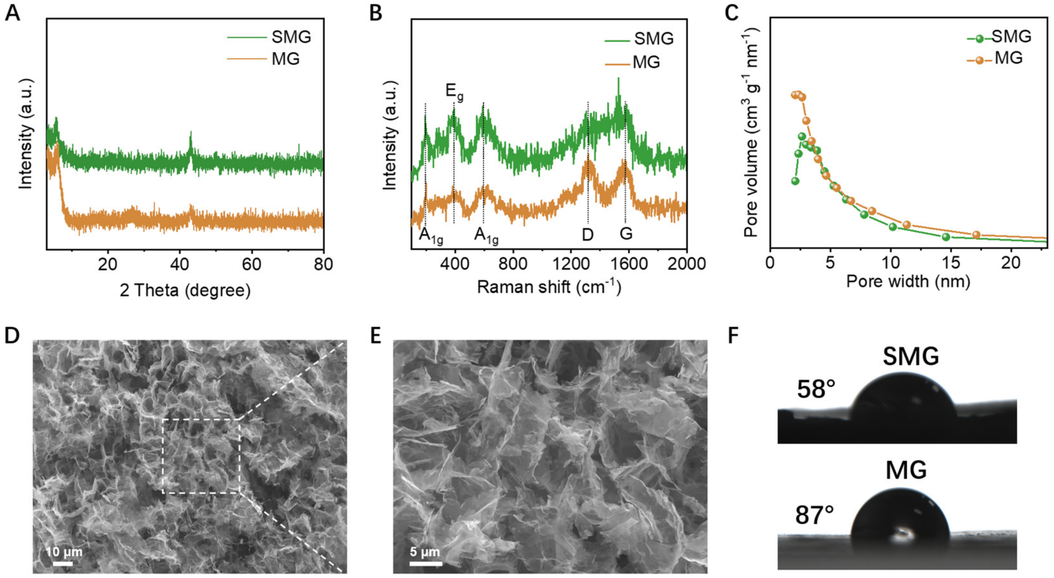

Fig. 4 Characterization of MG and SMG. (A) XRD, (B) Raman, and (C) pore size distributions of MG and SMG. (D and E) SEM images of SMG. (F) Electrolyte contact angles of MG and SMG.

GO on the surface of $Ti_3C_2T_x$ (Fig. 4D and E). Such wrinkles and the 3D structure are conducive to preventing the tight stacking of $Ti_3C_2T_x$. Furthermore, the electrolyte contact angle was measured to evaluate the benefits of the 3D porous structure and confirm its effective electrolyte penetration. As shown in Fig. 4F, SMG demonstrates a smaller electrolyte contact angle (58°) than MG (87°). This result strongly suggests that SMG possesses a more open structure, exhibiting superior wetting behavior and enabling rapid and efficient electrolyte penetration.[32,33]

The electrochemical performance of the samples was evaluated through the construction of ZHSCs, utilizing SMG or MG as the cathode, Zn foil as the anode, and an aqueous solution of 2 M $ZnSO_4$ as the electrolyte. Cyclic voltammetry (CV) and galvanostatic charge/discharge (GCD) measurements of the samples were systematically conducted between 0.2 and 1.1 V (*vs.* Zn^{2+}/Zn). During the discharging process, Zn metal is oxidized to Zn^{2+}, which is adsorbed on the cathode. Conversely, during the charging process, Zn^{2+} is reduced to Zn atoms and SO_4^{2-} is adsorbed on the surface of SMG or MG electrodes.[34,35] The CV profiles in Fig. 5A are indicative of both electric double layer behavior and pseudocapacitive behavior. Notably, SMG exhibits a larger CV curve area compared to MG, indicative of a superior specific capacitance. GCD measurements further confirm the superior capacity of SMG (Fig. 5B). As depicted in Fig. 5C and S11,† the areal specific capacitance derived from GCD data across various current densities reveals remarkable values of up to 526.2 mF cm^{-2} at 2 mA cm^{-2} and 98 mF cm^{-2} at 20 mA cm^{-2} for SMG, significantly outperforming MG (111.4 mF cm^{-2} and 4 mF cm^{-2}, respectively). Fig. S12† compares the Nyquist plots of the SMG and MG electrodes. A notably steeper slope in the low-frequency region is observed for the SMG electrode compared to the MG electrode. This observation suggests superior electrolyte ion diffusion within the SMG electrode, attributed to its improved surface accessibility, as corroborated by previous pore size distribution measurements. Additionally, it is noteworthy that the charge transfer impedance (R_{ct}) of SMG decreases to 121.4 Ω, compared to 41 031 Ω for MG, indicating enhanced charge transfer kinetics in the SMG electrode. Furthermore, variable scan-rate CV measurements within the range of 2 to 10 mV s^{-1} were conducted to gain deeper insight into the storage mechanism of the SMG electrode (Fig. S13†). According to the classical Randles–Sevcik equation,[36] the peak current (I_p) is proportional to the square root of the scan rate ($\nu^{1/2}$), which can be used to compare diffusion coefficients. Notably, by fitting the linear dependence of I_p *versus* $\nu^{1/2}$ (Fig. 5D and S14†), SMG demonstrated an excellent linear corre-

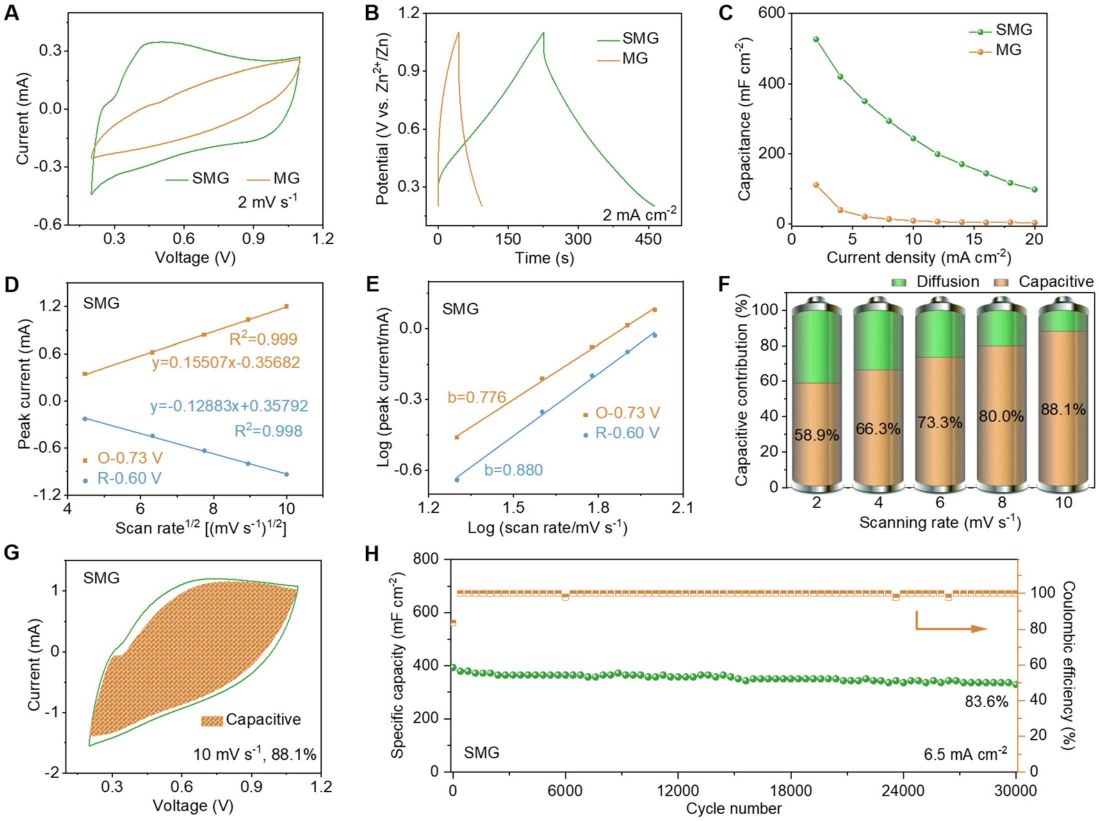

Fig. 5 (A) CV at 2.0 mV s^{-1} and (B) GCD curves at 2 mA cm^{-2} of MG and SMG electrodes. (C) Capacitance retention of SMG and MG at various current densities. (D) The linear relationship between the reductive (R) and oxidative (O) peak current (I_p) and the square root of the scan rate ($\nu^{1/2}$) for the SMG electrode. (E) The log(I_p) *vs.* log(ν) linear plots at the reductive (R) and oxidative (O) peaks of the SMG electrode. (F) Capacitance-contribution percentage at different scan rates of the SMG electrode. (G) CV curve of the SMG electrode at 10 mV s^{-1} with the estimated capacitive contribution shown in the orange region. (H) The long-term cycling performance of the SM electrode at 6.5 mA cm^{-2}.

lation accompanied by steeper slopes than MG, signifying superior diffusion characteristics. The SMG electrode exhibits a higher *b*-value compared to MG (as shown in Fig. 5E and S15†), indicating a favorable diffusion mechanism and enhanced intercalation pseudocapacitive behavior. Furthermore, quantitative analysis of capacitive contributions was performed at varying scan rates from 2 to 10 mV s^{-1} (Fig. 5F and S16†). Notably, SMG attains a capacitive-dominated contribution of 88.1% at 10 mV s^{-1}, markedly surpassing the 51.3% of MG (Fig. 5G and S17†). As shown in Fig. 5H, long-term cycling tests were performed. After 30 000 cycles at a current density of 6.5 mA cm^{-2}, the SMG electrode demonstrates remarkable electrochemical stability with 83.6% capacity retention, exhibiting a discharge capacity of 329.2 mF cm^{-2}. The initial coulombic efficiency of the SMG sample is 83.6%, which is primarily due to irreversible reactions between MXene surface functional groups (–OH, –F) and the electrolyte, as well as the formation of a solid electrolyte interphase (SEI) on the Zn anode during the first cycle, both of which consume active ions.[37,38] After few cycles, the coulombic efficiency stabilizes at ~99.9%. Compared to the MXene-based materials for zinc-ion storage reported in recent literature (Fig. S18†), the SMG electrode has demonstrated outstanding advantages in areal capacitance and capacitance retention. The detailed information is summarized in Table S1.†[39–44] Furthermore, the device exhibits an areal energy density of 59.20 μW h cm^{-2} (0.90 mW m^{-2}) and a power density of 8.92 mW cm^{-2} (11.03 μW h cm^{-2}) (Fig. S19†), which exceed those reported in recent literature (Table S2†).[40,41,45–50] These results further highlight the advantages of the obtained SMG aerogels in electrochemical zinc-ion storage.

Conclusions

In summary, under the protection of Na_2S, the storage life of $Ti_3C_2T_x$ is extended at temperatures of 25, 50, and 70 °C, as well as under visible light exposure. Furthermore, utilizing the reducing properties of Na_2S, the SMG aerogel was obtained by converting the suspension into a hydrogel at room temperature and then it was lyophilized. The SMG aerogel exhibited superior stability and outstanding antistacking ability because of the 3D structure, the unique pore structure of which is beneficial for enhancing charge-transport properties and promoting Zn^{2+} ion storage. A Zn//SMG ZHSC can achieve a high capacitance of 526.2 mF cm^{-2} at 2 mA cm^{-2} and retain an impressive capacity of 83.6% even after 30 000 cycles. These findings provide substantial insights into the rational development of antioxidants based on MXenes, thereby facilitating the rational design and preparation of MXene-based aerogels with enhanced stability and functionality.

Author contributions

Jie Wang: investigation, methodology, formal analysis, and writing – original draft. Guohao Li: visualization. Hailiang He: investigation and methodology. Xiaohui Li: data curation. Jiale Fan: investigation. Yingxinjie Wang: formal analysis. Xiuqiang Xie: validation, writing, and funding acquisition. Nan Zhang: funding acquisition, investigation, and supervision.

Data availability

Data will be made available on request.

Conflicts of interest

There are no conflicts to declare.

Acknowledgements

This work was supported by the National Natural Science Foundation of China (52272295, 52071137, 51977071, 51802040, and 21802020), the Science and Technology Innovation Program of Hunan Province (2021RC3066 and 2021RC3067), the Natural Science Foundation of Hunan Province (2020JJ3004), and the Graduate Research Innovation Project of Hunan Province (CX20240405). N. Zhang and X. Xie also acknowledge the financial support from the Fundamental Research Funds for the Central Universities. The Raman measurements were performed at the Analytical Instrumentation Center of Hunan University.

References

1 A. Lipatov, A. Goad, M. J. Loes, N. S. Vorobeva, J. Abourahma, Y. Gogotsi and A. Sinitskii, High electrical conductivity and breakdown current density of individual monolayer $Ti_3C_2T_x$ MXene flakes, *Matter*, 2021, **4**, 1413–1427.
2 J. Zou, J. Wu, Y. Wang, F. Deng, J. Jiang, Y. Zhang, S. Liu, N. Li, H. Zhang and J. Yu, Additive-mediated intercalation and surface modification of MXenes, *Chem. Soc. Rev.*, 2022, **51**, 2972–2990.
3 S. Zhao, Z. Liu, G. Xie, X. Guo, Z. Guo, F. Song, G. Li, C. Chen, X. Xie and N. Zhang, Achieving high–performance 3D K^+–pre–intercalated $Ti_3C_2T_x$ MXene for potassium–ion hybrid capacitors via regulating electrolyte solvation structure, *Angew. Chem., Int. Ed.*, 2021, **60**, 26246–26253.
4 X. Li, Z. Huang, C. E. Shuck, G. Liang, Y. Gogotsi and C. Zhi, MXene chemistry, electrochemistry and energy storage applications, *Nat. Rev. Chem.*, 2022, **6**, 389–404.
5 F. Wan, R. Liu, Y. Xia, K. Hu, Y. Lei, C. Wang, S. Zhang, S. Li, D. Yang, Y. Zheng and W. Chen, Phase-modified strongly coupled delta/epsilon-MnO_2 homojunction cathode for kinetics-enhanced zinc-ion batteries, *Inorg. Chem.*, 2024, **63**, 6988–6997.
6 Y. Li, J. Jiang, X. Li, M. Li, Y. Zheng and K. Sun, MXenes with functional N terminal group offer a covalent bond

storage mechanism for anions, *Phys. Rev. B*, 2024, **110**, 155401.

7 K. E. White, Y. Z. Chu, G. Gani, S. Ippolito, K. K. Barr, J. C. Thomas, A. Weber-Bargioni, K. C. Lau, Y. Gogotsi and P. S. Weiss, Atomic-scale investigations of $Ti_3C_2T_x$ MXene surfaces, *Matter*, 2024, **7**, 2609–2618.

8 M. Kramer, B. Favelukis, A. A. El-Zoka, M. Sokol, B. A. Rosen, N. Eliaz, S. H. Kim and B. Gault, Near-atomic-scale perspective on the oxidation of Ti3C2Tx, MXenes: insights from atom probe tomography, *Adv. Mater.*, 2024, **36**, e2305183.

9 R. A. Soomro, P. Zhang, B. Fan, Y. Wei and B. Xu, Progression in the oxidation stability of MXenes, *Nano-Micro Lett.*, 2023, **15**, 108.

10 X. Zhao, A. Vashisth, E. Prehn, W. Sun, S. A. Shah, T. Habib, Y. Chen, Z. Tan, J. L. Lutkenhaus, M. Radovic and M. J. Green, Antioxidants unlock shelf-stable $Ti_3C_2T_x$ (MXene) nanosheet dispersions, *Matter*, 2019, **1**, 513–526.

11 V. Natu, J. L. Hart, M. Sokol, H. Chiang, M. L. Taheri and M. W. Barsoum, Edge capping of 2D-MXene sheets with polyanionic salts to mitigate oxidation in aqueous colloidal suspensions, *Angew. Chem., Int. Ed.*, 2019, **58**, 12655–12660.

12 X. Wang, Z. Wang and J. Qiu, Stabilizing MXene by hydration chemistry in aqueous solution, *Angew. Chem., Int. Ed.*, 2021, **60**, 26587–26591.

13 Y. Zheng, Y. Wang, D. Liu, J. Zhao and Y. Li, Unlocking self–antioxidant capability and processability of additive–free MXene ink towards high–performance customizable supercapacitors, *Angew. Chem., Int. Ed.*, 2025, **64**, e202415742.

14 J. Wang, G. Xie, C. Yu, L. Peng, Y. Zhu, X. Xie and N. Zhang, Stabilizing $Ti_3C_2T_x$ in a water medium under multiple environmental conditions by scavenging oxidative free radicals, *Chem. Mater.*, 2022, **34**, 9517–9526.

15 J. Wang, G. Li, G. Xie, Z. Huang, P. Zhang, B. Xu, X. Xie and N. Zhang, Solvation structure design for stabilizing MXene in transition metal ion solutions, *SusMat*, 2024, e202.

16 S. F. Shaikh, R. S. Mane, B. K. Min, Y. J. Hwang and O.-s. Joo, D-sorbitol-induced phase control of TiO_2 nanoparticles and its application for dye-sensitized solar cells, *Sci. Rep.*, 2016, **6**, 1–10.

17 J. Wang, Y. Hu, B. Yang, X. Wang, J. Qin and M. Cao, Mechanochemistry-induced biaxial compressive strain engineering in MXenes for boosting lithium storage kinetics, *Nano Energy*, 2021, **87**, 106053.

18 H. Chen, Y. Wen, Y. Qi, Q. Zhao, L. Qu and C. Li, Pristine titanium carbide MXene films with environmentally stable conductivity and superior mechanical strength, *Adv. Funct. Mater.*, 2020, **30**, 1906996.

19 T. Habib, X. Zhao, S. A. Shah, Y. Chen, W. Sun, H. An, J. L. Lutkenhaus, M. Radovic and M. J. Green, Oxidation stability of $Ti_3C_2T_x$ MXene nanosheets in solvents and composite films, *npj 2D Mater. Appl.*, 2019, **3**, 8.

20 X. Zhao, A. Vashisth, J. W. Blivin, Z. Tan, D. E. Holta, V. Kotasthane, S. A. Shah, T. Habib, S. Liu, J. L. Lutkenhaus, M. Radovic and M. J. Green, pH, nanosheet concentration, and antioxidant affect the oxidation of $Ti_3C_2T_x$ and Ti_2CT_x MXene dispersions, *Adv. Mater. Interfaces*, 2020, **7**, 2000845.

21 H. Zhao, J. Ding, M. Zhou and H. Yu, Air-stable titanium carbide MXene nanosheets for corrosion protection, *ACS Appl. Nano Mater.*, 2021, **4**, 3075–3086.

22 T. Shang, Z. Lin, C. Qi, X. Liu, P. Li, Y. Tao, Z. Wu, D. Li, P. Simon and Q. H. Yang, 3D macroscopic architectures from self–assembled MXene hydrogels, *Adv. Funct. Mater.*, 2019, **29**, 1903960.

23 J. Hu, F. Song, S. Lian, Z. Liu, X. Peng, J. Wang, G. Li, Z. Wu, X. Xie and N. Zhang, Room-temperature assembled 3D macro-porous $Ti_3C_2T_x$/RGO hybrid hydrogel and the application as the self-standing electrode for sodium-ion storage, *J. Colloid Interface Sci.*, 2023, **650**, 1225–1234.

24 M. Fernández-Merino, L. Guardia, J. Paredes, S. Villar-Rodil, P. Fernández, A. Martínez-Alonso and J. Tascón, Vitamin C as an innocuous and safe reductant for the preparation of graphene suspensions from graphite oxide, *J. Phys. Chem. C*, 2010, **114**, 6426–6432.

25 L. M. Malard, M. A. Pimenta, G. Dresselhaus and M. S. Dresselhaus, Raman spectroscopy in graphene, *Phys. Rep.*, 2009, **473**, 51–87.

26 L. Li, M. Zhang, X. Zhang and Z. Zhang, New Ti_3C_2 aerogel as promising negative electrode materials for asymmetric supercapacitors, *J. Power Sources*, 2017, **364**, 234–241.

27 S. Stankovich, D. A. Dikin, R. D. Piner, K. A. Kohlhaas, A. Kleinhammes, Y. Jia, Y. Wu, S. T. Nguyen and R. S. Ruoff, Synthesis of graphene-based nanosheets via chemical reduction of exfoliated graphite oxide, *Carbon*, 2007, **45**, 1558–1565.

28 X. Wang, R.-J. Ma, T. Guo, X. Zhang, H. Wang and X. Zhao, S-TiO_2/Ti as efficient and stable electrocatalysts electrode for decomposition of HI to produce hydrogen, *J. Mater. Sci.*, 2023, **58**, 15035–15046.

29 T. Lei, Y. Xie, X. Wang, S. Miao, J. Xiong and C. Yan, TiO_2 feather duster as effective polysulfides restrictor for enhanced electrochemical kinetics in lithium–sulfur batteries, *Small*, 2017, **13**, 1701013.

30 S. Pei, J. Zhao, J. Du, W. Ren and H.-M. Cheng, Direct reduction of graphene oxide films into highly conductive and flexible graphene films by hydrohalic acids, *Carbon*, 2010, **48**, 4466–4474.

31 S. Pei and H.-M. Cheng, The reduction of graphene oxide, *Carbon*, 2012, **50**, 3210–3228.

32 J. Kim, W.-H. Khoh, B.-H. Wee and J.-D. Hong, Fabrication of flexible reduced graphene oxide-TiO_2 freestanding films for supercapacitor application, *RSC Adv.*, 2015, **5**, 9904–9911.

33 G. Li, J. Wang, H. Wu, F. Song, K. Tang, Z. Wu, X. Xie and N. Zhang, 3D isotropic MXene films enabling minimized polarization for enhanced sodium-ion storage performance, *Energy Storage Mater.*, 2024, **68**, 103327.

34 Y.-Q. Peng, M. Zhao, Z.-X. Chen, Q. Cheng, Y. Liu, X.-Y. Li, Y.-W. Song, B.-Q. Li and J.-Q. Huang, Boosting sulfur redox kinetics by a pentacenetetrone redox mediator for high-

energy-density lithium-sulfur batteries, *Nano Res.*, 2022, **16**, 8253–8259.

35 H. Luo, J. Jiang, Arramel, M. Li, K. Sun and Y. Zheng, Working mechanism of MXene as the anode protection layer of aqueous zinc-ion batteries, *J. Colloid Interface Sci.*, 2024, **654**, 289–299.

36 X. Rui, N. Yesibolati, S. Li, C. Yuan and C. Chen, Determination of the chemical diffusion coefficient of Li^+ in intercalation-type $Li_3V_2(PO_4)_3$ anode material, *Solid State Ionics*, 2011, **187**, 58–63.

37 X. Wang, X. Li, H. Fan and L. Ma, Solid electrolyte interface in Zn-based battery systems, *Nano-Micro Lett.*, 2022, **14**, 205.

38 Y. Guan, R. Zhao, K. Li, K. Chen, H. Zhu, X. Li, Q. Zhang, N. Yang, Z. Dong and G. Yuan, Tailoring surface chemistry of MXenes to boost initial coulombic efficiency for lithium storage, *Appl. Surf. Sci.*, 2023, **612**, 155875.

39 W. Tian, A. VahidMohammadi, M. S. Reid, Z. Wang, L. Ouyang, J. Erlandsson, T. Pettersson, L. Wågberg, M. Beidaghi and M. M. Hamedi, Multifunctional nano–composites with high strength and capacitance using 2D MXene and 1D nanocellulose, *Adv. Mater.*, 2019, **31**, 1902977.

40 L. Li, W. Liu, K. Jiang, D. Chen, F. Qu and G. Shen, *In situ* annealed $Ti_3C_2T_x$ MXene based all-solid-state flexible Zn-ion hybrid micro supercapacitor array with enhanced stability, *Nano-Micro Lett.*, 2021, **13**, 1–11.

41 S. Abdolhosseinzadeh, R. Schneider, A. Verma, J. Heier, F. Nüesch and C. Zhang, Turning trash into treasure: additive free MXene sediment inks for screen–printed micro–supercapacitors, *Adv. Mater.*, 2020, **32**, 2000716.

42 X. Tian, S. Zhao, Y. Gao, H. Li, W. Cao and B. Xu, 3D printing–directed synergistic design of high–performance zinc–ion hybrid capacitors and nanogenerators for all–in–one self–powered energy wristband, *Adv. Funct. Mater.*, 2023, **33**, 2300381.

43 M. Wang, Y. Cheng, H. Zhang, F. Cheng, Y. Wang, T. Huang, Z. Wei, Y. Zhang, B. Ge and Y. Ma, Nature–inspired interconnected macro/meso/micro–porous MXene electrode, *Adv. Funct. Mater.*, 2023, **33**, 2211199.

44 J. Xiao, J. Wen, J. Zhao, X. Ma, H. Gao and X. Zhang, A safe etching route to synthesize highly crystalline Nb_2CT_x MXene for high performance asymmetric supercapacitor applications, *Electrochim. Acta*, 2020, **337**, 135803.

45 P. Das, X. Shi, Q. Fu and Z. S. Wu, Substrate–free and shapeless planar micro–supercapacitors, *Adv. Funct. Mater.*, 2020, **30**, 1908758.

46 H. Zhang, Z. Wei, J. Wu, F. Cheng, Y. Ma, W. Liu, Y. Cheng, Y. Lin, N. Liu and Y. Gao, Interlayer-spacing-regulated MXene/rGO foam for multi-functional zinc-ion microcapacitors, *Energy Storage Mater.*, 2022, **50**, 444–453.

47 X. Li, H. Li, X. Fan, X. Shi and J. Liang, 3D–printed stretchable micro–supercapacitor with remarkable areal performance, *Adv. Energy Mater.*, 2020, **10**, 1903794.

48 S. Zheng, H. Wang, P. Das, Y. Zhang, Y. Cao, J. Ma, S. Liu and Z. S. Wu, Multitasking MXene inks enable high–performance printable microelectrochemical energy storage devices for all–flexible self–powered integrated systems, *Adv. Mater.*, 2021, **33**, 2005449.

49 X. Li, Y. Ma, Y. Yue, G. Li, C. Zhang, M. Cao, Y. Xiong, J. Zou, Y. Zhou and Y. Gao, A flexible Zn-ion hybrid micro-supercapacitor based on MXene anode and V_2O_5 cathode with high capacitance, *Chem. Eng. J.*, 2022, **428**, 130965.

50 C. Zhang, M. P. Kremer, A. Seral-Ascaso, S. H. Park, N. McEvoy, B. Anasori, Y. Gogotsi and V. Nicolosi, Stamping of flexible, coplanar micro–supercapacitors using MXene inks, *Adv. Funct. Mater.*, 2018, **28**, 1705506.